Article

Characterization of Pore Structure in Metal–Organic Framework by Small-Angle X-ray Scattering

Cheng-Si Tsao, Ming-Sheng Yu, Tsui-Yun Chung, Hsiu-Chu Wu, Cheng-Yu Wang, Kuei-Sen Chang, and Hsin-Lung Chen

J. Am. Chem. Soc., **2007**, 129 (51), 15997-16004 • DOI: 10.1021/ja0752336

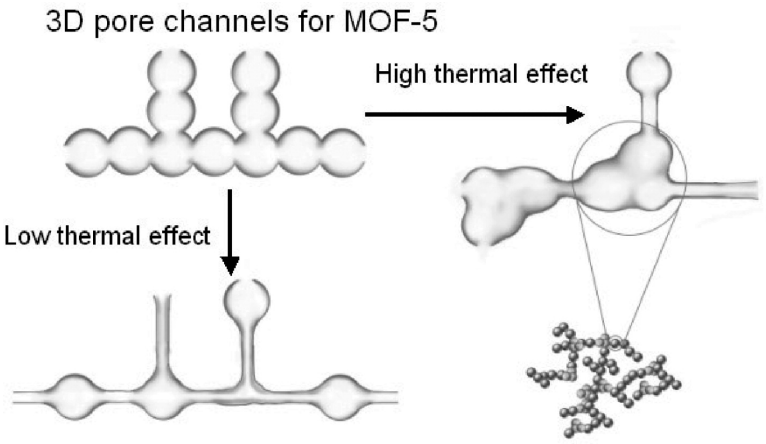

More About This Article

Additional resources and features associated with this article are available within the HTML version:

- Supporting Information
- Links to the 1 articles that cite this article, as of the time of this article download
- Access to high resolution figures
- Links to articles and content related to this article
- Copyright permission to reproduce figures and/or text from this article

View the Full Text HTML

J|A|C|S
ARTICLES
Published on Web 11/29/2007

Characterization of Pore Structure in Metal−Organic Framework by Small-Angle X-ray Scattering

Cheng-Si Tsao,*,† Ming-Sheng Yu,† Tsui-Yun Chung,† Hsiu-Chu Wu,† Cheng-Yu Wang,† Kuei-Sen Chang,† and Hsin-Lung Chen‡

Institute of Nuclear Energy Research, Longtan 32546, Taiwan, and Department of Chemical Engineering, National Tsing-Hua University, Hsin-Chu 300, Taiwan

Received July 13, 2007; E-mail: cstsao@iner.gov.tw

Abstract: MOF-5-like crystals were studied by small-angle X-ray scattering (SAXS) to reveal, both quantitatively and qualitatively, their real structural details, including pore surface characteristics, pore shape, size distribution, specific surface area (SSA), spatial distribution, and pore−network structure. A combined SAXS and wide-angle X-ray scattering (WAXS) experiment was conducted to investigate the variation of the pore structure with the MOF-5 crystalline phase produced at different cooling rates. The SSA of the MOF-5 crystals synthesized herein spanned a broad range from ∼3100 to 800 m^2/g. The real pore structures were divided into two regimes. In regime I the material consisted mainly of micropores of radius ∼8 Å as well as mesopores of radius 120∼80 Å. The structure in regime II was a fractal network of aggregated mesopores with radius ≥32 Å as the monomer, reducing SSA and hydrogen uptake capacity at room temperature. The two regimes can be manipulated by controlling the synthesis parameters. The concurrent evolution of pore structure and crystalline phase during heating for solvent removal was also revealed by the in-situ SAXS/WAXS measurement. The understanding of the impact of the real pore structure on the properties is important to establish a favorable synthetic approach for markedly improving the hydrogen storage capacity of MOF-5.

Introduction

Materials that can store large amounts of hydrogen at ambient temperature and relatively low pressures with small volume and fast kinetics have been a critical focus of work to support fuel-cell vehicle and portable electronic applications. None of the materials developed thus far satisfies the target criteria set by the U.S. Department of Energy. Recently, a new class of crystalline materials, referred to as metal−organic frameworks (MOFs),[1−7] have been identified as potential candidates for hydrogen storage.[5−7] The framework built from the linkage of metal clusters with the organic units (reticular synthesis) is an open 3D network which allows effective adsorption of hydrogen into its interior space. Ideally, a 3D channel structure[7−9] of MOF consisting of mutually orthogonal and perfectly ordered microporous 1D open channels (so-called pore channel[10]) would result in a high specific surface area (SSA) and micropore volume. For instance, the well-known MOF-5 consists of metal clusters $[Zn_4O(CO_2)_6]$ (as the corners of the unit cells) joined by benzene dicarboxylate (BDC) linkers to form an extended 3D simple cubic topology with intersecting pores with a 8 Å aperture width and a 12 Å pore diameter[2] (They are pseudospheres within the intersection of three mutually orthogonal pore channels). Notably, the structure of the MOF family, including the dimensions, shape, and volume of the pores, can be systematically tuned using diverse organic linkers to modify and improve hydrogen storage capacity.[7,11,12] Among the reported series of MOF, MOF-5 is the most stable and most porous and has been frequently considered as a potential commercialized target.[6,10]

† Institute of Nuclear Energy Research.
‡ National Tsing-Hua University.

(1) (a) Li, H.; Eddaoudi, M.; O'Keeffe, M.; Yaghi, O. M. *Nature* **1999**, *402*, 276−279. (b) Chae, H. K.; Siberio-perez, D. Y.; Kim, J.; Go, Y.-B.; Eddaoudi, M.; Matzger, A. J.; O'Keefe, M.; Yaghi, O. M. *Nature* **2004**, *427*, 523−527. (c) Rowsell, J. L. C.; Millward, A. R.; Park, K. S.; Yaghi, O. M. *J. Am. Chem. Soc.* **2004**, *126*, 5666−5667. (d) Dybtsev, D. N.; Chun, H.; Yoon, S. H.; Kim, D.; Kim, K. *J. Am. Chem. Soc.* **2004**, *126*, 32−33. (e) Lee, E. Y.; Jang, S. Y.; Suh, M. P. J. *J. Am. Chem. Soc.* **2005**, *127*, 6374−6381. (f) Eddaoudi, M.; Li, H.; Yaghi, O. M. *J. Am. Chem. Soc.* **2000**, 122, 1391−1397. (g) Chen, B.; Ockwig, N. W.; Millward, A. R.; Contreras, D. S.; Yaghi, O. M. *Angew. Chem., Int. Ed.* **2005**, *44*, 4745−4749. (h) Li, H.; Eddaoudi, M.; Groy, T. L.; Yaghi, O. M. *J. Am. Chem. Soc.* **1998**, *120*, 8571−8572.
(2) Yaghi, O. M.; O'Keeffe, M.; Ockwig, N. W.; Chae, H. K.; Eddaoudi, M.; Kim, J. *Nature* **2003**, *423*, 705−714.
(3) (a) Panella, B.; Hirscher, M. *Adv. Mater.* **2005**, *17*, 538−541. (b) Li, Y.; Yang, R. T. *J. Am. Chem. Soc.* **2005**, *128*, 726−727. (c) Li, Y.; Yang, R. T. *J. Am. Chem. Soc.* **2006**, *128*, 8136−8137.
(4) Panella, B.; Hirscher, M.; Pütter, H.; Müller, U. *Adv. Funct. Mater.* **2006**, *16*, 520−524.
(5) Rosi, N. L.; Eckert, J.; Eddaoudi, M.; Vodak, D. T.; Kim, J.; O'Keeffe, M.; Yaghi, O. M. *Science* **2003**, *300*, 1127−1129.
(6) Rowsell, J. L. C.; Eckert, J.; Yaghi, O. M. *J. Am. Chem. Soc.* **2005**, *127*, 14904−14910.
(7) Pan, L.; Sander, M. B.; Huang, X.; Li, J.; Smith, M.; Bittner, E.; Bockrath, B.; Johnson, J. K. *J. Am. Chem. Soc.* **2004**, *126*, 1308−1309.
(8) Lee, J.-Y.; Li, J.; Jagiello, J. *J. Solid State Chem.* **2005**, *178*, 2527−2532.
(9) Vishnyakov, A.; Ravikovitch, P. I.; Neimark, A. V.; Bulow, M.; Wang, Q. M. *Nano Lett.* **2003**, *3*, 713−718.
(10) Huang, L.; Wang, H.; Chen, J.; Wang, Z.; Sun, J.; Zhao, D.; Yan, Y. *Microporous Mesoporous Mater.* **2003**, *58*, 105−114.
(11) Eddaoudi, M.; Kim, J.; Rosi, N.; Vodak, D.; Wachter, J.; O'Keeffe, M.; Yaghi, O. M. *Science* **2002**, *295*, 469−472.
(12) Rowsell, J. L. C.; Yaghi, O. M. *Angew. Chem., Int. Ed.* **2005**, *44*, 4670−4679.

In the past few years, a broad set of procedures for MOF-5 synthesis has been reported. MOF-5 crystallites with Langmuir SSA $\geq$ 3000 m^2/g have been synthesized on the basis of the methods of Hirscher's[4] and Yaghi's[11] groups using *N,N′*-diethylformamide (DEF) as the solvent. For large-scale and fast synthesis at low cost, Huang et al.[10] and other groups[3] adopted *N,N′*-dimethylformamide (DMF) as an alternative solvent. The resultant MOF-5 samples were found to have much lower SSA (in the range ~1300 to 600 m^2/g). Indeed, substantial variation (from 600 to 3400 m^2/g) in the SSA values of the synthesized products, described as MOF-5 phase, has been observed. With regard to this issue, a recent work[13] by Hafizovic et al. provided a useful way to evaluate quickly (identify the phase of) MOF-5 materials from powder X-ray diffraction (PXRD) patterns. The experimental PXRD patterns obtained from the high-SSA MOF-5 by Hirscher's[4] and Yaghi's groups were consistent with calculated pattern.[10,13] However, the experimental PXRD patterns of the low-SSA samples synthesized by Hafizovic,[13] Huang,[10] and other groups[3] displayed a rather pronounced difference in the relative peak intensities, and some samples even demonstrated peak splitting. Hafizovic[13] et al. attributed this deviation to (1) the presence of $Zn(OH)_2$ species which partly occupied the cavities of the MOF-5 framework (the dominant phase) and (2) the minor phase consisting of doubly interpenetrated MOF-5 framework. Both resulted in pore-filling effects and thus reduced the available pore volume. Hafizovic et al. only identified such crystallographic defects of MOF-5 with low SSA.

Establishing the relationship between the structure and the storage capacity is key to guide the further rational design and synthesis of MOF materials with high hydrogen storage capacity. The maximum hydrogen storage capacity is closely related to the SSA of the adsorbent. However, SSA is not only one of the factors that govern the hydrogen storage of microporous MOF materials. Many studies[4,12] have pointed out that smaller pores enable the more effective use of the available pore volume for storing hydrogen. Therefore, tailoring or minimizing the size of most of the actual pores may be key to the optimal design of MOFs. Most studies have focused on the design of architecture and topology on the molecular level. In fact, none of synthetic methods can yield the perfect MOF crystal with theoretically maximum micropore density (or SSA). The real pore structure and pore network (defined as pore quality herein) thus deviate considerably from the ideal architecture. No experimental attempt has been made to reveal the real pore structure and pore network and understand how the synthetic conditions affect these structures. The real pore quality of MOF certainly exerts a strong influence on hydrogen storage capacity and SSA determination. Additionally, investigating the relationship between the real pore structure and the MOF crystalline phase identified by PXRD is complementary to the earlier work by Hafizovic et al.

This work presents combined small-angle X-ray scattering[14] (SAXS) and wide-angle X-ray scattering (WAXS) to resolve the real pore structure of MOF-5. The SAXS is a very powerful tool for disclosing crucial information on pore surface characteristics, pore shape, pore size distribution and volume, spatial distribution, and even pore−network structure. The SAXS result yields insight into the structures of real pores and their network responsible for hydrogen storage from the micropore scale ($\leq$2 nm) to the mesopore scale (between 2 and 50 nm). Traditionally, sorption isotherms of nitrogen or other gases have been used to evaluate the SSA and pore volume of MOF materials. This technique is however inappropriate for microporous materials because of the effect of closed porosity and diffusion hindrance.[15] Other inherent drawbacks and the assumptions that underlie the analytical models may also cause large error,[4] depending on the complexity of the porosity. Therefore, the structural parameters obtained by gas adsorption analysis must be validated or independently confirmed by SAXS for highly porous materials.[15] A comparison between the results obtained by nitrogen sorption and SAXS will thus be presented herein to assess the accuracy of gas adsorption measurements of the pores in MOF materials. Furthermore, this work will demonstrate the evolution of the pore structure in MOF as a function of various factors in synthesis. A combined SAXS and WAXS experiment is performed to establish the simultaneous relationship between pore structure and MOF-5 crystalline phase. Finally, an in-situ SAXS/WAXS experiment demonstrates the effect of temperature on the concurrent evolutions of pore structure and crystal phase during the removal of solvent upon heating. The results obtained herein are very helpful in identifying favorable synthetic conditions for significantly improving hydrogen storage capacity.

With respect to the MOF-5 materials used for the study, a high-quality MOF-5 crystal with SSA of ~3100 m^2/g was synthesized using DEF solvent using the methods reported by Hirscher's[4] and Yaghi's[11] groups. MOF-5 samples were also prepared using DMF as the solvent by the method of Huang et al.,[10] Hafizovic et al.,[13] Yang et al., [3b,c] and other groups. In this case, MOF-5 crystals with SSA from ~1200 to 850 m^2/g were obtained by manipulating the cooling rate of DMF solutions. In addition to these two classes of MOF-5, another MOF-5 material with intermediate SSA was produced for systematic comparison. The high-quality MOF-5 materials prepared herein are similar to the typical MOF-5 material originally prepared by Yaghi et al. because of the high-SSA characteristic and the same PXRD pattern. Rigorously speaking, these materials are not identical to MOF-5 material of Yaghi owing to their polycrystalline morphology, and should hence be described as "MOF-5-like" rather than "MOF-5". The hydrogen uptakes of the synthesized MOF-5 samples at room temperature (rt) and 6.9 MPa were measured. The correlation between the rt hydrogen-uptake capacity and the pore structure will be discussed.

Experimental Section

Synthesis of MOF-5. With respect to the batch of samples prepared with different cooling rates, 3.92 g of $Zn(NO_3)_2 \cdot 4H_2O$ and 0.83 g of H_2BDC were directly added to 130 cm^3 of DMF solvent. After sufficient

(13) Hafizovic, J.; Bjφrgen, M.; Olsbye, U.; Dietzel, P. D. C.; Bordiga, S.; Prestipino, C.; Lamberti, C.; Lillerud, K. P. *J. Am. Chem. Soc.* **2007**, *129*, 3612−3620.

(14) (a) Glatter, O.; Kratky, O. *Small-Angle X-Ray Scattering*; Academic Press: London, 1982. (b) Guinier, A.; Fournet, G. *Small-Angle Scattering of X-Rays*; Wiley: New York, 1955. (c) Tsao, C.-S.; Chang, H.-L.; Jeng, U.-S.; Lin, J.-M.; Lin, T.-L. *Polymer* **2005**, *46*, 8430−8437. (d) Tsao, C.-S.; Chen, C.-Y.; Jeng, U.-S.; Kuo, T.-Y. *Acta Mater.* **2006**, *54*, 4621−4631. (e) Tsao, C.-S.; Chen, H.-L. *Macromolecules* **2004**, *37*, 8984−8991.

(15) (a) Francoise, E.-D.; David, F.-J.; Sandrine, B.-F.; Patrick, A.; Francoise, B.; Francisco, C.-M.; David, D.; Carlos, M.-C.; Isabelle, M. *Carbon* **2005**, *43*, 3009−3012. (b) Sandrine, B.-F.; David, L.; Patrick, A.; Daniel, C.; David, D.; Francoise, E.-D. *J. Non-Cryst. Solids* **2004**, *350*, 136−144. (c) Bock V.; Emmerling, A.; Saliger, R.; Fricke *J. Porous Mater.* **1997**, 4, 287−294. (d) Smarsly, B.; Göltner, C.; Antonietti, M.; Ruland, W.; Hoinkis, E. *J. Phys. Chem. B* **2001**, *105*, 831−840.

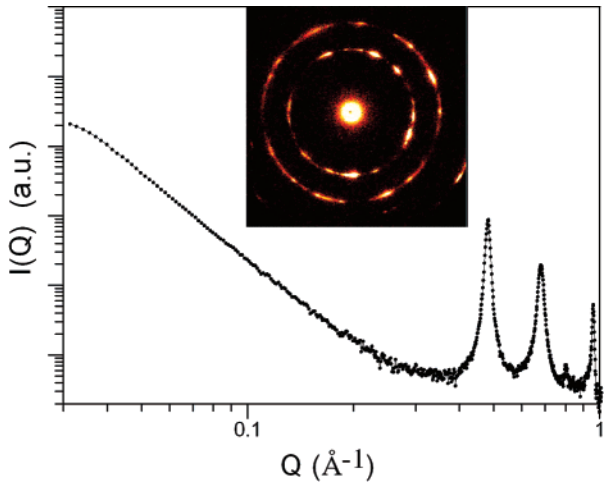

Figure 1. Combined SAXS/WAXS profile for high-SSA MOF-5_H crystal as an example. (The inset shows a 2D scattering pattern with rings that correspond to the first three diffraction peaks.)

stirring, the DMF solution was heated to 130 °C for 4 h in a refluxing system and then cooled to rt. The cooling rate was controlled using temperature controller. The solid product was filtered off and then washed in DMF three times before $CHCl_3$-exchange was applied. The MOF-5-like crystals with relatively low SSA (denoted as MOF-5_L) were synthesized at four cooling rates: 5 °C/min, 0.5 °C/min, 0.2 °C/min, and 0.05 °C/min. These samples were activated under a reduced vacuum at 125 °C for 3 h. The crystal with SSA ≥ 3100 m^2/g (denoted as MOF-5_H) was prepared by adding 1.56 g of $Zn(NO_3)_2 \cdot 4H_2O$ and 0.33 g of H_2BDC to 50 cm^3 of DEF solvent. The remaining procedures were as above, except that the DEF solution was heated to ∼120 °C for 12 h and then cooled to rt at a cooling rate of ∼1.6 °C/min. Larger MOF-5_H crystals can also be prepared at rt for 1 month. Many crystals were also prepared from the DEF solutions at temperatures between rt and 130 °C for different periods. The SSA of this class of MOF-5-like (denoted as MOF-5_M) was between that of MOF-5_H and that of MOF-5_L.

Characterization Methods. The SAXS experiments were performed using a Bruker NANOSTAR SAXS instrument. Incident X-rays were generated using a rotating-copper target and the scattered intensity was collected using a 2D multiwire channel detector. The powderlike samples for SAXS measurements were sealed in airtight cells with Kapton windows. The collected SAXS data were corrected for transmission, dark current, and background, and averaged azimuthally as a function of the scattering vector Q, where $Q = 4\pi\lambda^{-1}\sin(\vartheta)$ and ϑ and λ are the scattering angle and the incident X-ray wavelength, respectively. The typically obtained SAXS intensity profiles covered the Q range 0.01∼0.3 $Å^{-1}$. A second SAXS configuration with the shortest sample-to-detector distance (29 cm) was adopted to extend the measured Q range toward higher Q values. The lattice constant of the crystalline phase of MOF-5 is relatively large, so this extended SAXS measurement, covering Q range from 0.04 to 1.0 $Å^{-1}$, also allowed the crystal diffraction patterns to be obtained (Figure 1). The combination of the scattering profiles collected from the two configurations yielded the combined SAXS/WAXS profiles with the full Q range of 0.01∼1.0 $Å^{-1}$. The PXRD pattern measured using a Bruker D8 diffractometer over a 2ϑ range of 5°∼50° was used to confirm the ordered crystalline structure of MOF-5. A Hitachi S800 scanning electron microscope (SEM) was employed to observe the morphology of MOF-5 crystal. Nitrogen sorption isotherms at 77 K (Micromeritics ASAP2020) were measured to assess the SSA, the pore size, and the pore volume of MOF-5. High-pressure thermal gravimetric analysis (HPTGA, Cahn Thermax 500) was performed to measure hydrogen uptake at rt and 6.9 MPa.

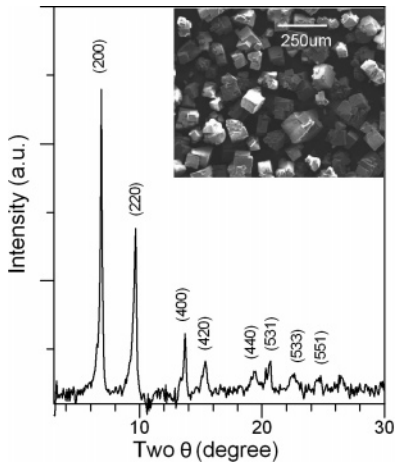

Figure 2. PXRD pattern measured for synthesized MOF-5-like crystal of SSA: ∼3100 m^2/g (Cu Kα radiation. Inset is SEM image of crystals.)

Results and Discussion

SEM observations indicate that almost all of the synthesized MOF-5 crystals are cubic with sides of 10∼100 μm. The PXRD pattern (Figure 2) of the MOF-5_H crystal with a Langmuir SSA of ∼3100 m^2/g (Table 1) is consistent with that of MOF-5 (SSA: 3840 m^2/g), reported by Hirscher's group.[4] This measured PXRD pattern also agrees well in both peak intensity and position with the calculated pattern[10,13] of the typical MOF-5 phase (*Fm3m* symmetry) with a lattice constant $a = 25.5$ Å, confirming the long-range ordered cubic structure. The XRD patterns (Figure 3b) of MOF-5_L crystals with SSA from ∼1200 to 850 m^2/g also agree with those of Huang,[10] Hafizovic,[13] and other groups.[3]

The measured nitrogen adsorption−desorption isotherms of all samples show a type-I profile with an initial sharp increase in the volumetric uptake (at low relative pressure p/p_o) followed by a plateau, which signifies micropore filling. In particular, MOF-5_L and MOF-5_M display a small hysteresis loop at $p/p_o > 0.45$ (the onset of capillary condensation), typically stemming from the mesoporosity. Similar hysteresis phenomena have been observed in other studies of MOF systems and are thought to originate from the intercrystalline voids in the sample.[8,9] Table 1 presents Brunauer−Emmet−Teller (BET) SSA, Langmuir SSA, mean pore volume and pore size, determined from the measured isotherms. The volume, size, and SSA of the micropores, as well as the mesopore SSA (also called the "external surface") were determined using the *t*-plot method and Horvath−Kawazoe (H−K) analysis. In summary, three classes of MOF-5 with high, medium, and low SSA (MOF-5_H, MOF-5_M and MOF-5_L, respectively) were prepared here.

Figure 3a displays the SAXS profiles of MOF-5_L crystals prepared at different cooling rates. The scattering pattern of the sample cooled at 5 °C/min is almost identical to that cooled at 0.5 °C/min. In contrast, the SAXS profile becomes dependent on the cooling rate for slower cooling at ≤0.2 °C/min. The observed SAXS profiles can thus be divided into two regimes with a crossover between 0.5 and 0.2 °C/min. The regimes that correspond to cooling rates of ≥0.5 °C/min or ≤0.2 °C/min are regime I and regime II, respectively. These two regimes represent different pore structures and properties. As will be discussed later, regime I is characteristic of the typical porous structure with spherical micropores and mesopores,[15c] while

Table 1. Structural Parameters of All MOF-5_H, _M, and _L Samples, Determined from Nitrogen Sorption Isotherms as Functions of Synthesis Factors

class (solvent/ heating, °C)	cooling rate (°C/min)	BET SSA (m^2/g)	Langmiur SSA (m^2/g)	micropore SSA[a] (m^2/g)	mesopore SSA[a] (m^2/g)	micropore volume[a] (cm^3/g)	average pore volume (cm^3/g)	median pore diameter[a] (Å)	average pore diameter[b] (Å)
H (DEF/120)	1.6	2766.5	3113.0	2353.0	413.5	0.952	1.404		20.0
M(DEF/rt∼130)	1.6		1200∼2500						
L (DMF/130)	5	1032.4	1180.7	940.4	91.9	0.373	0.421	9.4	16.3
L (DMF/130)	0.5	978.5	1107.5	886.7	91.8	0.355	0.406	9.4	16.6
L (DMF/130)	0.2	862.1	977.1	779.6	82.6	0.313	0.357	9.3	16.6
L (DMF/130)	0.05	755.1	844.7	687.1	68.0	0.272	0.309	9.4	16.4

[a] Based on the *t*-plot method and H−K analysis. [b] Based on 4 × volume/surface by BET method.

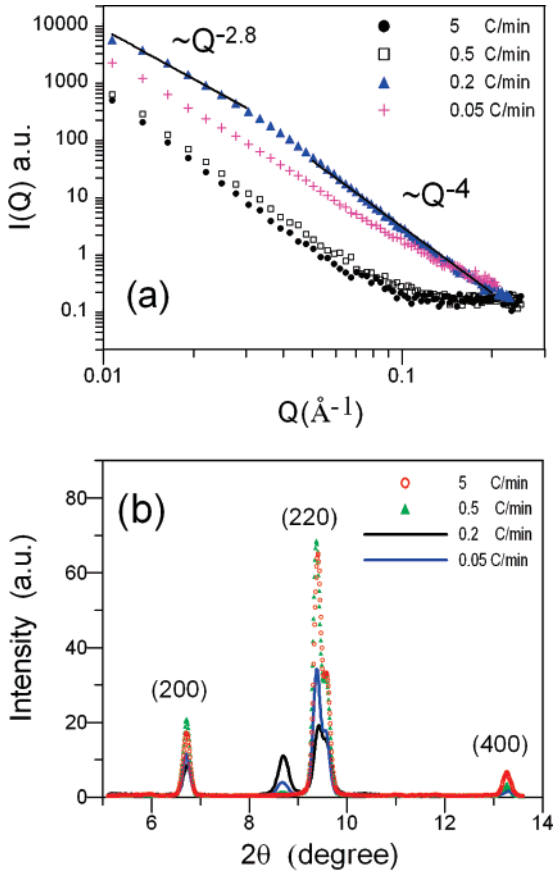

Figure 3. (a) Cooling-rate-dependent SAXS profiles and (b) corresponding WAXS profiles of MOF-5_L crystals prepared from DMF solution at cooling rates of 5 °C/min, 0.5 °C/min, 0.2 °C/min, and 0.05 °C/min, respectively. The SAXS and WAXS profiles measured simultaneously show two regimes.

regime II exhibits the characteristic fractal network[16] that is formed by the aggregation of mesopores as the monomer. Notably, the nanostructure in regime I has significantly higher BET and Langmuir SSA values than that in regime II, according to Table 1.

The SAXS profiles of regime I (Figure 3a) displays power-law scattering of Q^{-4} in the low-Q region ($0.01 < Q < 0.08$ Å^{-1}), which corresponds to the asymptotic scattering behavior[14a,d] of larger pores or mesopores. Prior to the quantitative fitting of the observed intensity profiles, all SAXS curves were further

(16) (a) Emmerling, A.; Fricke, J. *J. Non-Cryst. Solids* **1992**, *145*, 113−120. (b) Schaefer, D. W. *Science* **1989**, *243*, 1023−1027. (c) Schaefer, D. W.; Martin, J. E. *Phys. Rev. Lett.* **1984**, *52*, 2371−2374. (d) Roe, R. J. *Methods of X-Ray and Neutron Scattering in Polymer Science*; Oxford University Press: New York, 2000.

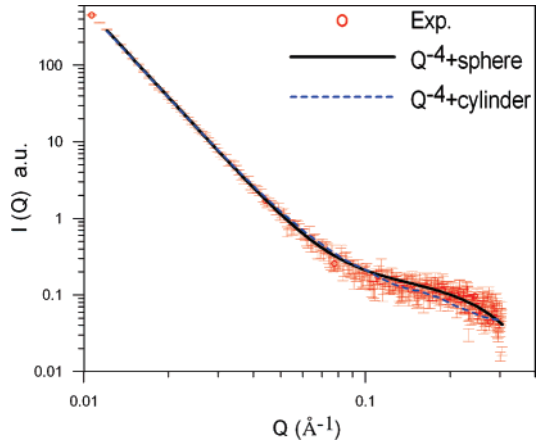

Figure 4. Background-subtracted SAXS profile of MOF-5_L sample with cooling rate of ∼5 °C/min, fitted using Q^{-4} + sphere model (solid line) and Q^{-4} + infinite cylinder model (dashed line), respectively.

subtracted by the background obtained by extrapolating the shoulder of the WAXS diffraction peak in the higher-Q region ($0.3 < Q < 0.5$ Å^{-1}). A form factor profile, contributed to mainly by the micropores, becomes visible at $0.1 < Q < 0.3$ Å^{-1} after this subtraction (Figure 4). Therefore, the SAXS intensity of regime I is modeled with

$$I(Q) = AQ^{-4} + \eta(\Delta\rho)^2 V_p P(Q) \qquad (1)$$

where the first term, with a constant A, describes the smooth surface (or sharp boundary) effect of the mesopores, which contribute most to the low-Q intensity. The second term represents the form factor scattering from the spherical micropores: $\Delta\rho$, η, and V_P are the difference between the scattering length densities of the pores and the solid-state matrix, the micropore volume fraction, and the micropore volume, respectively. The form factor $P(Q)$ of spherical micropores of radius R is given by[14a,c]

$$P(Q) = \left[3\frac{\sin(QR) - QR\cos(QR)}{(QR)^3}\right]^2 \qquad (2)$$

Equation 1 provides a good fit to the observed SAXS profile (Figure 4). The fitted radii R, ∼8 Å, (Table 2) are consistent with the two reported pore radii of 6 [2,11] and 9 Å,[1a] estimated from the atomic Van der Waals radii within the unit-cell, verifying the pore architecture in the unit-cell model. Notably, the scattering peak (structure factor) associated with the interaction between pores is not observed in the measured SAXS profile, indicating that the micropores are randomly dispersed

Table 2. Structural Parameters Determined by SAXS Technique and Hydrogen Storage Capacity at rt and 6.9 MPa

crystal class	cooling rate (°C/min)	regime	R_{micro}[a] (Å)	R_{meso}[a] (Å)	SSA fraction of micropores	H_2 uptake (wt %)
MOF−5_H	1.6	I	6.9	81	0.82	0.27
MOF−5_L	5	I	8.3	120	0.96	0.27
MOF−5_L	0.5	I	8.4	125	0.95	0.29
MOF−5_L	0.2	II				0.24
MOF−5_L	0.05	II				0.19

[a] R_{micro} and R_{meso} are the model-fitted radii of micropores and mesopores, respectively.

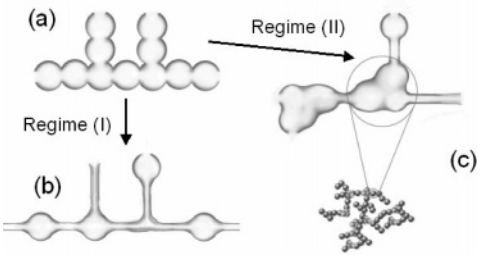

Figure 5. Simple schematic (a) ideal model of pores in cubic 3D channel structure; (b) real structure with disordered spherical micropores interconnected by fine channels; and (c) real fractal network formed by aggregation of mesopores by Ostwald coarsening of micropores.

and not spatially ordered. We propose that the well-separated pores are still connected to each other through the long channels, maintaining the open-pore characteristic (Figure 5). These putative (long and narrow) channels are too few to be detected by SAXS, given the number density and volume of the mesopores; they may be formed by the collapse of pores due to the imperfect formation of real crystals with much lower pore volume. Since the topology of MOF-5 is cubic, all ideal pore channels intersect mutually in three orthogonal directions. Forming simple infinite (with a certain orientation) or wormlike cylindrical pore channels in a real MOF-5 crystal is very difficult. To confirm the absence of the infinite cylindrical pore channels, an infinite cylinder form factor[14b,d,e] (dashed curve in Figure 4) was used to fit the SAXS profile. The results reveal that the sphere form factor yields a much better fit than the cylinder model. The radius fitted using the infinite cylinder form factor is ∼5 Å. Although this value is close to the aperture radius in the pore channel that is estimated from the MOF-5 topology, our fittings of the SAXS profiles indicate that the micropores are present in the form of well-separated spheres without distinct spatial order. Notably, the error bars on the SAXS data in the high-Q region ($0.1 < Q < 0.3$ Å^{-1}) are 15∼20%; therefore, sphere form factor fitting yields only a rough mean approximation of the shape and dimensions of the micropores.

For micropores with sharp and smooth pore−solid interfaces, the SAXS profile manifests power-law scattering of $I(Q) \propto Q^{-4}$ in the high-Q region, allowing the model-independent determination of the surface-to-volume ratio Σ using the Porod law[14a,c,16d]

$$\lim_{Q\to\infty} Q^4 I(Q) = K = 2\pi(\Delta\rho)^2\Sigma \qquad (3)$$

where the constant K is the asymptotic value determined from the high-Q intensity. The SAXS profile in Figure 4 can be resolved into two components associated with the mesopores and the micropores. According to eqs 1 and 3, the SSA ratio of micropores to mesopores can be regarded as the ratio of Σ values of these two pores, and be determined from the ratio of the determined asymptotic values that correspond to the micropores and mesopores, respectively (K/A ratio). However, this ratio, determined by the Porod law in this work, is subject to error that results from the mesopores and macropores larger than 50 nm, as they are undetectable by the present SAXS configuration because of the limit in the minimum accessible Q value. The SSA fraction of the micropores calculated from the ratio of the experimental asymptotic values (Table 2) exceeds 90%, revealing the dominance of the micropore SSA in regime I. This fact is consistent with the result derived from the gas adsorption measurement.

The Q^{-4}-dependent intensity in the low-Q region, contributed to by the mesopores, may also be fitted using the sphere form factor. The radius obtained from this fit (∼ 120 Å) is only a very rough estimate, considering the large error that arises from the extrapolation fitting. Notably, the BJH mean mesopore diameter determined by gas adsorption measurement is ∼30 Å. This value is probably wrong because mesopores with diameters of ∼30 Å cannot produce a Q^{-4}-dependent intensity in the low-Q region of the SAXS profiles.

The SAXS profiles in regime II exhibit two distinct regions of power-law scattering on the respective length scales, as displayed in Figures 3a. This scattering pattern can be interpreted in terms of the fractal structure,[16] where an open network with a branched and self-similar appearance is formed by the aggregation of the pores as the monomer. In the low-Q region of $0.01 < Q < 0.04$ Å^{-1}, the SAXS intensity decreases as $I(Q) \propto Q^{-D}$, where exponent D corresponds to the mass fractal dimension of the network structure. The power law behavior $I(Q) \propto Q^{D_s-6}$ in the high-Q region can be attributed to the surface morphology of the monomers or the individual pores, where D_s is the fractal dimension of the surface. A smooth surface with D_s value of 2 leads to a power law of Q^{-4} (the Porod law), while a fractally rough surface with $D_s = 2\sim3$ causes a less steep intensity decay. Crossover between the mass and surface fractal regions occurs at the scattering vector (Q_c), which corresponds to the reciprocal of the radius of gyration R_g of the constituent pores ($Q_c^{-1} = R_g$). The radius of a spherical pore can then be calculated using the relationship $R = 1.29R_g$. The slopes of the measured SAXS profiles in Figure 3a reveal a mass fractal dimension of 2.8∼2.9 for the network structure, followed by Porod behavior in the high-Q region, indicating a smooth pore surface. The pore radius of MOF-5_L samples with a low cooling rate (≤0.2 °C/min) is thus determined to be 32.3 Å from the crossovers at 0.04 Å^{-1}.

The reason why pores become larger (in the mesopore scale) and aggregate to form fractal network in regime II is now discussed. The low cooling rate gives the system sufficient time at high temperatures, at where the solid-state atomic diffusion is enhanced or substantially accelerated. In this case, the well-known Ostwald ripening mechanism plays a significant role in the coarsening kinetics of pore formation. Emmerling and Fricke[16a] reported that the formation of fractal structure in some aerogels is related to Ostwald ripening. The driving force of Ostwald coarsening is the reduction of surface free energy, which can be achieved by the shrinkage of aperture windows at the intersection between pores. Therefore, the coarsening of the pores can be regarded as the coalescence of adjacent pores

(Figure 5). Further aggregation of the coarsening pores eventually generates a fractal network.

While the mesopores were revealed by SAXS, SEM observations show that numerous larger pores (including intercrystalline voids) of hundreds of Angstroms in size are present between the fine crystal grains within the powder particles. The formation of such large pores may be related to the fractal structure and pore coalescence. Notably, gas sorption analysis failed to reflect structural details in regime II, as it yielded pore diameters in the micropore range. The *t*-plot method for determining the mespore SSA and micropore volume does not offer sufficient resolution for the observed mesopores (radii of 32.3 Å).

On the basis of our SEM observations, the rough sizes of polycrystalline MOF-5 powders with SSA of ~3000, 1200, and 850 m^2/g are ~100, ~50, and ~10 μm, respectively. The sizes of the highly oriented crystal grains inside each sample also depend on the polycrystalline crystal morphology. These highly oriented crystal grains observed by 2D WAXS pattern are generally 0.2 to a few μm in size. Because of the limited minimum Q value (at 0.01 $Å^{-1}$), Porod scattering from the crystal grains and their surface roughness does not contribute to the SAXS profile. The mesopore density is usually maximal at the intercrystal space because the system approaches the lower free energy. Therefore, the intercrystal roughness/space is likely to correspond to the scale of the aggregated mesopores or macropore.

In summary, two regimes with different pore morphologies, depending on the cooling rate used for sample preparation, were identified. Increasing cooling rate causes a transition from regime II to regime I at a crossover between 0.5 and 0.2 °C/min. The pore structure formed in regime I is stable with respect to a change in cooling rate. At low cooling rate (≤0.2 °C/min), the fractal structure develops substantially as the cooling rate in regime II decreases, resulting in cooling-rate-dependent SSA and H_2 uptake. Observations suggest that high-quality MOF with high SSA and H_2 uptake capacity can be synthesized by forming the regime I morphology as the cooling rate increases.

The WAXS profiles in Figure 3b, which were collected simultaneously with the SAXS profiles in Figure 3a, reveal that the relative intensities of the peaks at 6.9° and 9.7° are inverted, unlike the calculated and previously reported XRD patterns of the MOF with high SSA. The observed WAXS pattern is however consistent with that reported by Huang,[10] Hafizovic,[13] and Yang[3b] for MOFs with lower SSA. The deviation from the calculated profile may be attributed to the pore-filling effect that is associated with the presence of Zn species and solvent, as well as lattice interpenetration in the nanocavities.[13] Notably, a transition of the WAXS pattern, characterized by the splitting of the 9.7° peak and a drop in peak intensity, occurs in parallel with a transition in the pore structure from regime I to regime II. Hafizovic,[13] et al. pointed out that both the peak splitting phenomenon and the change in relative peak intensities (at 6.9° and 9.7°) are attributable to the slight distortion of the MOF-5 lattice cell and the symmetry change from cubic to trigonal. The variation in WAXS profiles observed herein thus indicates that the loss of both the long-range order and the symmetry of the typical cubic MOF-5 phase are closely related to the pore coarsening and the fractal structure in regime II. The correlation between the characteristics of lattice distortion/defects and the mesopore evolution is evident. On the other hand, there was a

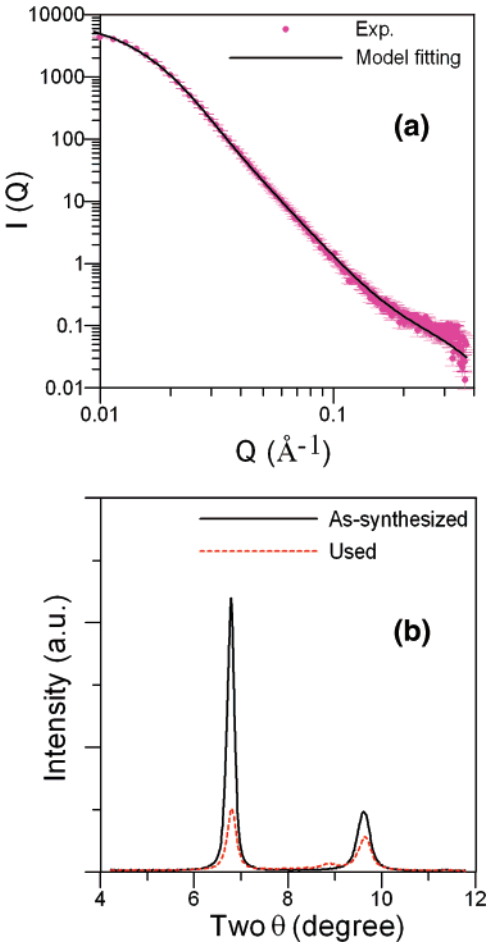

Figure 6. (a) Background-subtracted SAXS profile of typical MOF-5_H crystal fitted with bimodal size distribution model. Error bars of SAXS intensities in the range $0.2 < Q < 0.4$ $Å^{-1}$ are 15~20%. (b) WAXS profiles of as-synthesized and used MOF-5_H crystals as example.

different explanation for the peak splitting phenomenon at 9~10°. The PXRD pattern in Huang's work[10] (Figure 5 in ref 13, for MOCP-H material) indicated that the additional peak at ~9° was associated with water molecules that are weakly bound with the metal clusters of MOF-5 during crystal formation.

Hafizovic[13] et al. proposed a rational interpretation for the large variation in SSA, which is accompanied by peak splitting and pronounced changes in diffraction peak intensities. Indeed, the decrease in SSA measured herein from ~1200 to ~900 m^2/g (see Table 1) is accompanied by these two perturbations of the WAXS pattern. Hafizovic[13] et al. also claimed that the presence of Zn species and framework interpenetration in the nanocavities effectively reduced the pore volume of the materials. However, other factors may also determine the hydrogen storage capacity at 77 K. For instance, the MOF-5 samples prepared by Hirscher et al.[3a] and Yang et al.[3b,c] exhibited Langmuir SSAs of 1000 ~1300 m^2/g and PXRD patterns that are consistent with those of Huang,[10] Hafizovic,[13] and this work. The hydrogen storage capacities measured at 77 K for these samples were still sufficiently high to agree with the latest results from Yaghi's group[1c] for the high-SSA MOF-5. The present work complementarily suggests that pore structure and the crystal lattice defect are also related to variations in hydrogen uptake. MOF-5 with a regime II pore structure will later be demonstrated to lead to a lower rt hydrogen uptake than in SSA.

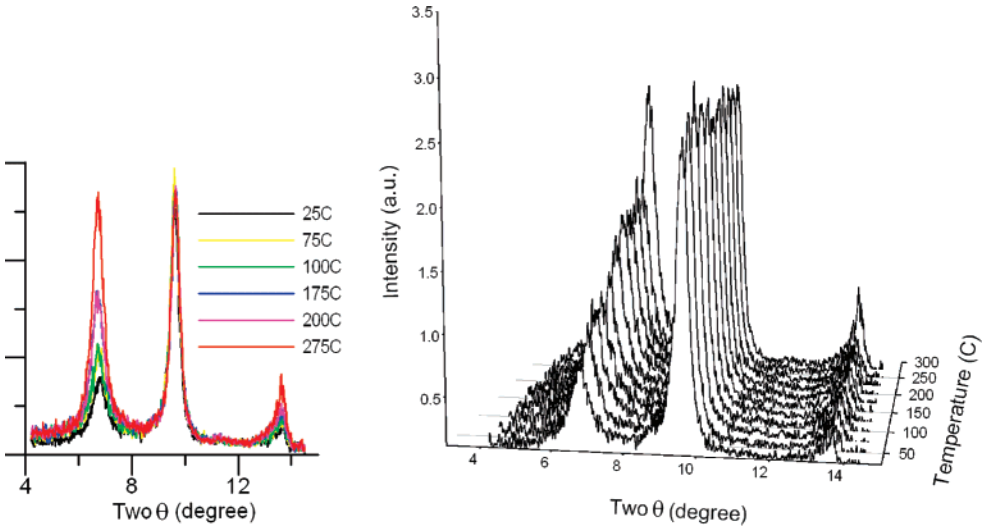

Figure 7. Temperature-resolved WAXS profiles of MOF-5_M crystal during heating from 25∼275 °C to remove solvent. The left part displays two saturations of increasing evolution of the 6.9° peak intensities at 75 and 175 °C, respectively.

The SAXS profile (Figure 6a) of MOF-5_H crystals with Langmuir SSA of ∼3100 m^2/g is characteristic of the regime I pore structure, consisting of micropores and mesopores. Here, the SAXS intensity has a Guinier region in the low-Q region (∼0.012 $Å^{-1}$) followed by the power-law decay of Q^{-4}, which is contributed to by the sharp interface of the corresponding mesopores. A typical form factor scattering profile contributed mainly by the micropores is also observed at $0.2 < Q < 0.4$ $Å^{-1}$. The existence of the Guinier region shows that the mesopores are much smaller and no interaction exists between these well-separated pores. The SAXS profiles ($Q < 0.2$ $Å^{-1}$) associated with the mesopores can be modeled on the basis of the polydisperse sphere form factor with a Schulz-size distribution. When the contribution of the micropores is also considered, the SAXS profiles are entirely fitted by a bimodal model that comprises a polydisperse sphere form factor for mesopores and a monodispersed sphere form factor for micropores described in eq 2. The fitted radii of the mesopores have a mean R_c of 81 Å and a polydispersity p of 0.45. The polydispersity p is defined as σ/R_c, where σ is the variance of the Schulz-size distribution. The fitted radius of the micropores is ∼7 Å (Table 2) and is consistent with the previously estimated value. Basically, the sizes of the mesopores in MOF-5_H are much closer to the radius of micropores than MOF-5_L and this fact explains the high SSA value. Gas adsorption measurements cannot easily differentiate mesopores from micropores because their sizes are similar. The smaller mesopore size is closely related to the presence of the high-symmetry cubic phase (which can be compared with the WAXS pattern in Figure 6b). The small mesopores observed herein may also indicate a much less collapsed channel formation.

Figure 6b displays the WAXS profiles of as-synthesized and "used" MOF-5_H crystals. The "used" MOF-5_H crystal is the sample that has undergone prolonged degas at 200 °C followed by adsorption−desorption isotherm measurement. Both WAXS profiles have relative peak intensities and peak positions that are consistent with the calculated PXRD pattern of the typical MOF-5 phase, demonstrating the good thermal stability of the synthesized MOF-5 material.

The rt hydrogen uptake is relatively low owing to the dilute monolayer adsorbed at rt.[3a] Besides the temperature effect, this study reveals that the formation of many narrow channels collapsed from the pore structure may be unfavorable to the sufficient monolayer adsorption of hydrogen molecules. Hirscher[3a] et al. reported that the rt hydrogen uptake at 6.7 MPa for MOF-5 with Langmuir SSA of ∼1000 m^2/g was ∼0.16 wt %. Their recent work[4] further demonstrated that the MOF-5 sample with Langmuir SSA of ∼3800 m^2/g had a slightly higher rt hydrogen uptake of 0.28 wt % at 6.5 MPa. Nevertheless, the maximum accessible hydrogen uptake at rt and 6.7 MPa for MOF-5 with a lower Langmuir SSA of ∼1300 m^2/g, as prepared by Yang's group,[3b,c] was ∼0.3 wt %. The hydrogen uptake capacities at rt and 6.9 MPa of MOF-5_H and L samples prepared herein agree with those in the cited studies (Table 2). Because the adsorbed amount is low, the average error bar is estimated to be ∼15%. According to our measurements and earlier results, the rt hydrogen uptakes at a given pressure for MOF-5 samples with SSAs from 3000 to 1000 m^2/g are almost independent of SSA within the error bar. Identifying a linear relationship between rt hydrogen uptake and SSA is therefore difficult. The pore structures of both MOF-5_H and L samples with SSA of over ∼1000 m^2/g (Table 2) are in regime I. In this case, the population of the mesopores increases with SSA. However, mesopore adsorption may disfavor rt hydrogen uptake, such that the uptake does not increase despite the significant increase of SSA. Table 2 also indicates (by a systematic trend) that the fractal network developed by mesopore coarsening in regime II clearly reduces rt hydrogen uptake.

MOF-5_M crystals with intermediate SSA are more frequently obtained than MOF-5_H over a wide range of temperatures and heating times. The WAXS pattern of the MOF-5_M crystal after complete removal of solvent and a further heating was similar to that of the MOF-5_H crystal. However, the peak intensity at 6.9° was slightly higher in intensity than that at 9.7° for MOF-5_M. In-situ SAXS/WAXS measurement was made on heating to reveal the effect of temperature on the structural evolutions of both the pores and the crystalline phase of MOF-5_M during the removal of residual DEF solvent after DEF washing and $CHCl_3$-exchange. The heating process was performed under vacuum from 25 to 275 °C in increments of 25 °C. The times for sample equilibration and data acquisition was 30 min at each temperature. The temperature-resolved

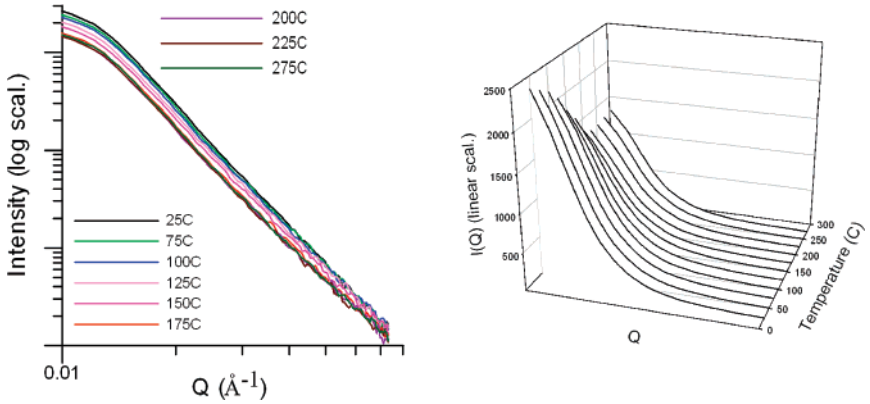

Figure 8. Temperature-resolved SAXS profiles, corresponding to Figure 7. (Left and right parts plot intensities on logarithmic and linear scales, respectively.)

WAXS profiles in Figure 7 show that the intensity of the 6.9° peak increases with the temperature (for solvent removal) because of the pore-filling effects. Meanwhile, the intensity of the 9.7° peak remains constant, a finding which is consistent with the study of Hafizovic[13] et al. on the solvent removal behavior. Two clear stages, characterized by saturations of the evolution of the first peak, are observed. The first stage occurred at ~75 °C and corresponds to the removal of adsorbed water. The intensity grows upon further heating from 75 °C, but it saturates again at the second stage near 175 °C, which represents the complete evacuation of the DEF molecules from pores. These two stages correspond well with the weight losses associated with solvent removal detected by TGA.[1h,13] Notably, the peak saturation observed in the temperature range of 175~250 °C reveals both the complete removal of all contained solvents and stable phase formation. A sharp increase of the 6.9° peak to the same height as the 9.7° peak is observed at ~270 °C, indicating enhanced crystalline ordering of MOF-5 due to the thermal effect. This enhanced ordering is also evidenced by the appearance of diffraction spots from the highly oriented crystals in the 2D WAXS pattern.

Figure 8 presents the SAXS profiles corresponding to the temperature-resolved WAXS profiles. Combining Figures 7 and 8 resolves the concurrent evolutions of pore and crystalline structure during the removal of solvent by heating. The SAXS profile at rt shows that the pore structure is in regime I and the size of the mesopores is between those of MOF-5_L and H crystals. The micropore radius (~8 Å) is however the same as those of MOF-5_L and MOF-5_H. The slope of power-law scattering in the intermediate-Q region ($0.02 < Q < 0.07$ Å^{-1}) gradually increases from −4.0 to −3.7 as the temperature increases from 25 to 175 °C. This slight variation suggests that the interface of mesopores changes from a sharp boundary to a diffusive boundary because of solvent removal. The profile shapes in the low- and high-Q regions ($0.01 < Q < 0.02$ Å^{-1} and $0.2 < Q < 0.4$ Å^{-1}, respectively) remain unchanged, revealing the stabilities of the radii of the mesopores and the micropores with respect to heating. Moreover, the SAXS intensities in the high-Q region (right part plot with Q region: $0.01 \sim 0.3$ Å^{-1}) measured at all temperatures merge into a curve, indicating that the volume fraction of the micropores is stable. The intensity at the lowest accessible Q of 0.01 Å^{-1} can be roughly regarded as the zero-angle intensity, $I(Q = 0)$, which is proportional to the volume fraction of the mesopores. This intensity decreases markedly as the temperature increases. The volume fraction loss of the mesopores in the temperature range 25~75 °C, that is associated with the desorption of water, is ~8%. The following loss between 75 and 175 °C is ~38% and is caused by the removal of organic solvent. The SAXS profiles in the temperature range 175~275 °C are almost the same, signaling the saturation of the structural evolution after complete removal of the solvent. Notably, the SAXS profiles at $T \geq 175$ °C show that the pore structure becomes stable and is hence not affected by the further ordering of the crystalline structure that is revealed by WAXS at 275 °C. The MOF-5_H crystal also exhibits similar pore behavior, which was observed using temperature-resolved SAXS during the removal of solvent. Consequently, the micropore structure is very stable regardless of the heating and degas processes. A fraction of the mesopore volume serves as a solvent accommodation site or an open flow path and collapses after the removal of the solvent under vacuum. The mesopores play an important role in the solvent-desorption activity inside the crystal, as evidenced by the temperature-resolved SAXS profiles, and may be related to the rt hydrogen storage activity.

JA0752336